Volume 1 | Number 1 | Jan 2013 | Pages 1–100

Nanoscale

www.rsc.org/nanoscale

ROYAL SOCIETY OF CHEMISTRY

ROYAL SOCIETY OF CHEMISTRY

www.rsc.org/nanoscale

Journal Name

ARTICLE

Chemically-doped graphene with improved surface plasmon characteristics: an optical near-field study

Zebo Zheng,[ad] Weiliang Wang,[d] Teng Ma,[c] Zexiang Deng,[d] Yanlin Ke,[ab] Runze Zhan,[a] Qionghui Zou,[ad] Wencai Ren,[c] Jun Chen,[ab] Juncong She,[ab] Yu Zhang,[ab] Fei Liu,[ab] Huanjun Chen,[ab*] Shaozhi Deng,[ab*] Ningsheng Xu[ab]

One of the most fascinating and important merits of graphene plasmonics is their tunability in a wide range. While chemical doping has been proven to be a facile and effective way for such a purpose, most of the previous studies focused on the macroscopic behaviors of the plasmons in chemically-doped graphene, and little was known about their nanoscale responses as well as related mechanisms. Here, to the best of our knowledge, we presented the first experimental near-field optical study on chemically-doped graphene with improved surface plasmon characteristics. By using a scattering-type scanning near-field optical microscope (s-SNOM), we managed to show that the graphene plasmons can be tuned and improved using facile chemical doping method. Specifically, the plasmon interference patterns near the edge of monolayer graphene were substantially enhanced *via* nitric acid (HNO$_3$) exposure. The plasmon-related characteristics can be deduced by analyzing such plasmonic fringes, which exhibited a longer plasmon wavelength and reduced plasmon damping rate. In addition, the local carrier density and therefore the Fermi energy level (E_F) of graphene can be obtained from the plasmonic nano-imaging, which indicated that the enhanced plasmon oscillation was originated from the injection of free holes into the graphene from the HNO$_3$. These findings were further corroborated by theoretical calculations using density functional theory (DFT). We believe that our findings have provided a clear nanoscale picture on improving graphene plasmonics by chemical doping, which will be helpful on one hand for optimizing graphene plasmonics, and on the other hand for elucidating the mechanisms of two-dimensional light confinement by atomically thick materials.

1 Introduction

As an atomic thick material with extreme light confinement, strong optical responses, and broad electronic and optoelectronic tunability, graphene has gained substantial attention in the past decade not only in scientific research but also in industrial applications.[1–3] Many of the graphene's fascinating optical and optoelectronic properties stem from its surface plasmons, the surface electromagnetic wave associated with the collective Dirac electron oscillation.[4–7] Under light excitation with proper configurations the two-dimensional electron gas in the graphene will be polarized, whereby surface plasmons can be initiated and propagate along the graphene surface. Due to the unique electronic band structure of graphene, the plasmons has been demonstrated to exhibit unprecedented spatial confinement with broadband

response up to mid-infrared region.[8–10] These distinct characteristics have made graphene outstanding platform for light focusing and manipulation in two dimension,[11,12] which can benefit the applications in optical communication,[13,14] optical sensing and imaging,[15,16] and optical data storage.[17]

One fascinating merits of the graphene is that its electrical and optical properties are amenable to wide-range tuning by adjusting the charge carrier density, whereby the plasmon-related characteristics can be tailored *via* external doping. On the other hand, although theoretical calculations predicted an ultra-long in-plane propagation distance (tens to 100 plasmon wavelengths) for the graphene plasmon,[8,11,18] the values revealed by most of the experimental results on pristine graphene are much smaller (only several plasmon wavelengths).[19–22] Such a discrepancy is due to strong plasmon losses induced by defects in the graphene, coupling with the substrate phonons, as well as other adsorbates onto the graphene. These plasmon losses have placed great hurdles for real applications of graphene plasmon in future optoelectronic devices. In view of these, how to tailor the graphene plasmon and reduce its damping therefore become two of the most important issues in nowadays graphene plasmonics research. A variety of studies have proposed several strategies to meet these two issues. For example, electrostatic gating was demonstrated as an efficient manner for continuously tuning the graphene plasmon wavelengths and oscillation strengths.[20,23] Optical excitation was introduced for ultrafast control of the graphene plasmon responses.[24,25] In a very recent study, the graphene plasmon wavelength can be tailored into the near-infrared regime by taking advantage of the hole doping from MoO$_3$ film coated onto the graphene.[25] To reduce the plasmon losses, an ultrathin film inserted between the graphene

a. *State Key Laboratory of Optoelectronic Materials and Technologies, Guangdong Province Key Laboratory of Display Material and Technology, Sun Yat-sen University, Guangzhou 510275, China.*
b. *School of Electronics and Information Technology, Sun Yat-sen University, Guangzhou 510006, China.*
c. *Shenyang National Laboratory for Materials Science, Institute of Metal Research, Chinese Academy of Sciences, 72 Wenhua Road, Shenyang 110016, China.*
d. *School of Physics, Sun Yat-sen University, Guangzhou 510275, China*

* *Corresponding Authors: chenhj8@mail.sysu.edu.cn; stsdsz@mail.sysu.edu.cn*
†Electronic Supplementary Information (ESI) available: Optical image and AFM topography of the HNO3-doped graphene, XPS spectra of the pristine and HNO$_3$-doped graphene, Plasmon wavelengths deduced from different data normalization methods, additional optical near-field characteristics of the graphene before and after the HNO$_3$ doping, binding energies of the H$_2$O molecule on the graphene. See DOI: 10.1039/x0xx00000x

and substrate can strongly suppress the coupling between graphene plasmon and substrate phonon and thereafter increase the plasmon propagation lengths.[26] Another strategy involved the quasi-suspended architecture where the graphene was lifted from the supported substrate.[27] In such a manner the plasmon damping due to the scattering by the substrate phonons can be strongly reduced.

Among these different strategies, chemical doping is of high interest as an efficient method for controlling and improving the graphene plasmon characteristics.[28–32] On one hand, the carrier density of the graphene can be modulated in a broad range by the chemical doping method,[32] and as a result the graphene plasmon characteristics can be tailored and enhanced. On the other hand, the chemical doping is facile to be implemented in comparison with its counterparts. The doping of charge carriers can even be achieved by simply exposing the graphene to dilute molecule vapor.

This is especially beneficial for large-area postprocessing and highthroughput occasions. During the past few years, chemical doping was widely utilized for tuning graphene plasmon wavelengths,[33] tailoring the plasmon response of stacked graphene nanostructures,[34] and enhancing the plasmonic terahertz response of the graphene films.[31] However, most of these studies mainly paid attention to the far-field macroscopic plasmon responses of the chemically-doped graphene. A study on the nanoscale behaviors, especially direct visualization of the graphene plasmons after chemical doping is as of yet unreported, although previous theoretical and experimental studies on metal nanostructures have clearly indicated the differences between plasmonic far-field and near-field behaviors.[35,36] Such a study can eliminate ensemble and inhomogeneous averaging, which can help for elucidating the intrinsic characteristics of plasmons in the chemically-doped graphene.
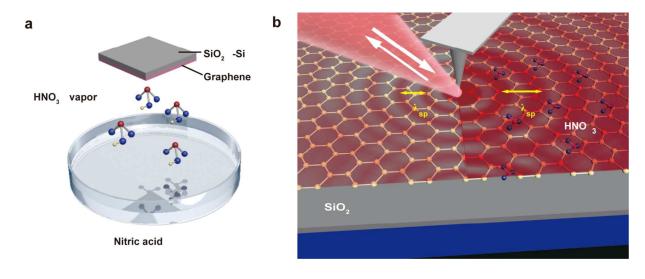

Fig. 1 Schematic showing the near-field study of plasmonic properties of the chemically-doped graphene. (a) Schematic showing the doping of graphene by the HNO₃ vapor, where the graphene was kept upside down above the HNO₃ solution (68% in volume). (b) Schematic showing the s-SNOM measurements of the graphene (Gr) on SiO₂. The two white arrows display the directions of incidence and back-scattered light, respectively. Concentric red circles demonstrate the plasmon waves propagating on the graphene surface. The two yellow double-headed arrows indicate the plasmon wavelengths on the pristine (left) and chemically-doped graphene (right), respectively.

Herein, by utilizing infrared nano-imaging technique, we presented the near-field optical study on chemically-doped graphene with improved surface plasmon characteristics. HNO₃ vapor was used to dope the graphene grown with chemical vapor deposition (CVD) method. The s-SNOM technique was then employed to directly image the plasmon propagation in HNO₃-doped graphene, with a spatial resolution down to 25 nm. The plasmon fringes near the graphene edge can thereafter be extracted, which allow for deriving the plasmon wavelengths, plasmon damping rates, and E_F. In comparison with the pristine graphene, the chemical doping can reduce the plasmon damping rate by ~ 34% and therefore enhance the plasmon strength. In addition, the chemically-doped graphene exhibited a longer plasmon wavelength. The extracted E_F agreed with the DFT results, which indicated that the improved plasmon characteristics were due to the injection of holes into the graphene from the HNO₃. Our study has provided a direct picture on the plasmons in chemically-doped graphene, which can help to understand the mechanisms

governing the improvement of graphene plasmon characteristics *via* chemical doping procedures.

2 Results and discussion

The single-crystalline graphene used in our study was grown by the CVD method.[37,38] Electrochemical bubbling transfer method was utilized to transfer the graphene onto silicon substrate with 290-nm-thick oxide layer (SiO₂).[37] The sample was further annealed in hydrogen ambience to remove the polymer residues on the graphene incorporated during the transfer process. The obtained graphene exhibited thicknesses around 0.7 ~ 0.9 nm (Fig. S1[†]). Fluctuations in the sample thicknesses can be ascribed to the variations in the contact between the samples and substrate, and polymer residues on the graphene surface. The silicon substrate with graphene was then exposed to HNO₃ vapor to induce the chemical doping

(Fig. 1a). To reveal the plasmonic properties of the chemically-doped graphene, s-SNOM was employed for imaging the optical near-field distributions.[39] In a specific measurement, a mid-infrared source was focused on the metal-coated tip with radius of ~ 25 nm (Fig. 1b). By demodulating the detected signal at a higher harmonic of the tip vibration frequency background-free near-field optical amplitude can be obtained.[39,40] In our current study we will employ the fourth harmonic, s_4. Due to the large in-plane momenta q launched

by the tip apex, the tip could compensate the momentum mismatch of free-space light and surface plasmon in the graphene.[40] The incidence optical field was strongly confined beneath the tip and launched the plasmon with wavelength of λ_{sp}. These radial propagating waves then formed periodic fringes owing to its interference with the edge-reflected waves (Fig. 1b). The plasmon strengths, plasmon damping rates, and plasmon wavelengths can then be extracted from the interference patterns.
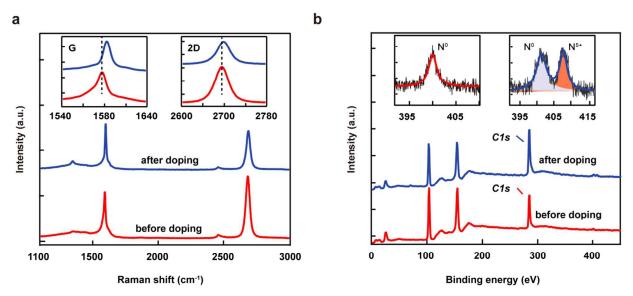

Fig. 2 Spectroscopy characterizations of the monolayer graphene. (a) Typical Raman spectra of the monolayer graphene before (red) and after (blue) the HNO_3 doping. Insets indicate the enlarge views of the G and 2D bands. (b) XPS spectra of the monolayer graphene before (red) and after (blue) the HNO_3 doping. Insets give the enlarge views of the nitrogen bonding states.

The HNO_3 has been demonstrated as a p-type dopant in graphitic materials.[41] When the monolayer graphene was exposed to the acid vapor, the HNO_3 molecules were randomly adsorbed onto the graphene surface and initiated the following reaction,[28,42]

$$6HNO_3 + 25C \rightarrow C_{25}^+ NO_3^- \cdot 4HNO_3 + NO_2 + H_2O \qquad (1)$$

As a result, C(O)OH, C–H, and NO_3^- were introduced into the graphene lattice through sp^2–sp^3 hybridization.[31,43] In such a manner the protonation process occurred where the electrons transferred from graphene to the HNO_3 molecules, leading to downshift of the E_F. The doping effects on the graphene electronic structure can be manifested by Raman spectroscopy. Fig. 2a gives the comparison of the Raman spectra from monolayer graphene before (red line) and after (blue line) exposed to the HNO_3 vapor. After doping the G band shifted from 1592 cm^{-1} to 1599 cm^{-1}, while the 2D band moved from 2685 cm^{-1} to 2689 cm^{-1}. Such blue-shift behaviors indicated a p-type doping and downward shift of the E_F.[43] In addition, the Raman band associated with the graphene defects at 1344 cm^{-1} became stronger after the HNO_3 exposure, suggesting breaking of C–C bond due to the sp^2–sp^3 hybridization. The specific E_F value can be obtained by considering the intensity ratio between 2D and G bands (I_G/I_{2D}), which is another important parameter that strongly depends on the charge carrier density. In our study the I_G/I_{2D} value for pristine graphene was 0.63, indicating an E_F around −0.25 eV relative

to the charge-neutral point of graphene.[44,45] The initial p-doping was caused by the SiO_2 substrate.[46] After doping HNO_3 the I_G/I_{2D} value increased to 1.06, which corresponded to an E_F of −0.57 ~ −0.70 eV.[44,45] This is consistent with an enhanced p-doping by the HNO_3.

The changes of the electronic structure in the graphene can further be revealed by X-ray photoelectron spectroscopy (XPS). As shown in Fig. 2b, with HNO_3 doping the C1s peak associated with the carbon sp^2 and sp^3 hybridization states shifted from ~284.58 eV to ~284.18 eV (Fig. S2[†]). Such an observation is consistent with previous results.[43] In addition, a weak N1s peak around 406.5 eV appeared in the doped sample (Fig. 2b, right inset), indicating formation of N^{5+} and therefore the NO_3^-. The weak intensity of the N1s peak suggests that the concentration of NO_3^- is extremely low with respect to the carbon atoms. One should note that a small peak at ~ 400.5 eV can be observed for the pristine and HNO_3-doped samples, which can be ascribed to the adsorbed nitrogen compound such as NOx from the surrounding environment.

The near-field plasmonic characteristics of the graphene were revealed using 10.70 μm mid-infrared light generated from a CO_2 laser as the excitation. The laser was focused onto a metal-coated atomic-force-microscope (AFM) tip to launch the plasmon polariton wave on the graphene surface. The plasmon wave will be reflected by the edges or grain boundaries of the graphene and interfere with the tip-

launched waves,[21] giving rise to fringes observed from the near-field optical signal (Fig. 1b). The plasmon wavelengths and damping rates can thereafter be obtained by investigating these fringes.
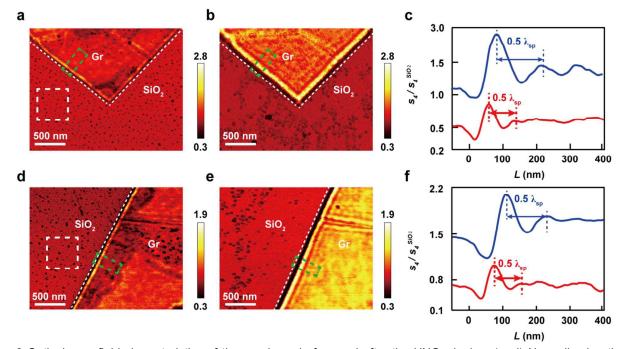

Fig. 3 Optical near-field characteristics of the graphene before and after the HNO$_3$ doping. (a, d) Normalized optical near-field imaging of the plasmon waves near edges of the pristine graphene. (b, e) Normalized optical near-field imaging of the plasmon waves near edges of the chemically-doped graphene. The graphene edges are marked by white dashed lines. The normalization was done *via* dividing every pixel by the average amplitude of the region enclosed by the white rectangle in each image. (c) Extracted profiles of the near-field optical amplitudes from green rectangles shown in (a) and (b). (f) Extracted profiles of the near-field optical amplitudes from green rectangles shown in (d) and (e). The blue (red) solid line indicates profile of chemically-doped (pristine) graphene. The profiles were obtained by averaging over 50 lines in the green rectangles.

To ensure that the near-field optical characterizations were measured on the same graphene before and after the chemical doping, we used the specific patterns of the graphene as markers to locate the sample under the AFM tip (Fig. S1a and b[†]). Fig. 3 gives the near-field optical characteristics of two representative pieces of graphene. In our study in order to remove the effects of the substrate for quantitative analysis, the near-field intensities were normalized to the SiO$_2$ substrate without the graphene. One should note that usually the material used for data normalization is gold due to its flat dispersion in the mid-infrared region.[47] However, the use of the SiO$_2$ for the data normalization will not disturb the results of our current study. In our study, we aim to demonstrate the effects of the HNO$_3$ doping on the plasmonic characteristics of the monolayer graphene. To this end we will focus on quantitatively comparing the plasmonic amplitudes and plasmon dispersion properties between the pristine and chemically-doped graphene. For the plasmonic amplitudes, monochromic laser was utilized as the excitation, whereby the intensities of the plasmon ripples on the pristine graphene were compared to those on the doped graphene. Therefore the data normalization was done at the specific laser line, which will not be disturbed by the strong dispersion of the SiO$_2$ substrate. On

the other hand, for the comparison of the plasmon dispersion properties, the plasmon wavelengths deduced from the near-field ripples will be inspected. Specifically, to obtain the plasmon dispersion we extracted optical near-field profiles with varied illumination wavelengths, whereby the plasmon wavelength λ_{sp} and corresponding wavevector q can be deduced. In such measurements we will concern about the separations between adjacent ripples while disregard the intensities of the ripples. In view of this, although the SiO$_2$ substrate exhibits much different responses under excitations of various wavelengths, the use of it for the data normalization will only affect the amplitudes of the plasmon ripples and leave the plasmon wavelengths undisturbed (Fig. S3[†]). Therefore the obtained plasmon dispersion properties will not be disturbed by the use of the SiO$_2$. A very recent study has also verified the validity of using the SiO$_2$ for the data normalization in the s-SNOM measurements.[48]

Due to the unintentional doping from the SiO$_2$ substrate, bright fringes induced by the plasmonic interference can be found near the edges or grain boundaries on pristine graphene (Fig. 3a and d). The fringes next to the edges exhibited highest intensities while those away from the edges decayed rapidly. Disappearance of the fringes was due to annihilation of the reflected plasmon waves by defects and impurities in the
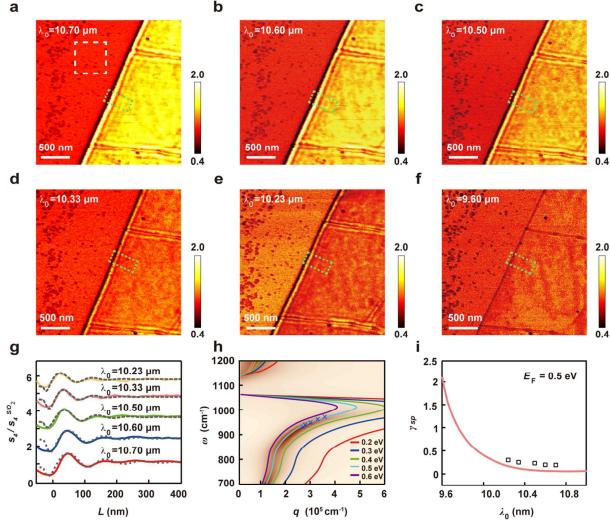
ARTICLE

graphene. In addition, the near-field distributions were non-uniform in regions away from the edges and grain boundaries, indicating the variations of electronic properties such as charge carrier densities and mobilities within the graphene flake. Such variations can be ascribed to the nonuniform impurity and defect distributions on the graphene surface.

After doped with the HNO_3 the optical near-filed amplitudes of the graphene were enhanced notably (Fig. 3b and e). The enhancement was more obvious from the near-field amplitude profiles perpendicular to the graphene edges in the area marked by the green rectangles shown in Fig. 3a and d. In

Fig. 4 Plasmon dispersion of the chemically-doped graphene. (a–f) Normalized optical near-field amplitude images taken using different excitation wavelengths λ_0. The normalization was done *via* dividing every pixel by the average amplitude of the region enclosed by the white rectangle in each image. (g) Extracted profiles of the near-field optical amplitudes from green rectangles shown in (a)–(f). Each profile was obtained by averaging over 50 lines in the green rectangle shown in the corresponding image. The dashed lines were fitting results using the cavity model. (h) Comparison between the experimental plasmon dispersion (blue crosses) and those calculated using the Drude-type conductivities with different E_F. The two dimensional pseudo-color background was obtained by calculating the imaginary part of the reflection coefficient $r_p(q,\omega)$. (i) Dependence of the plasmon damping rate, γ_{sp}, on the excitation wavelengths. Empty squares were obtained from the cavity model. The solid red line was obtained using the Drude-type conductivity of the monolayer graphene.

comparison with the pristine graphene, the brightest fringes in the doped graphene was strengthened by 12% ~ 51% (Fig. 3c and f). More insights on the graphene plasmon can be extracted from the intensity profiles. In addition to the improvements of the optical intensity, the number and width of the fringes on the chemically-doped graphene were enlarged. Increment in the fringe number suggests that the reflected plasmon waves from the graphene edges can propagate a longer distance on the graphene surface and

therefore interfere effectively with the tip-launched plasmon wave in the interior of the graphene. The long plasmon propagation lengths are due to reduction of the plasmon damping in the doped graphene. One can preliminarily evaluate the plasmon damping by calculating the ratio between the intensities of the first fringe next to the edge and inner part of the graphene where the fringes are faint.[27] Such an intensity ratio increased from 1.35 to 1.87 by chemical doping, which clearly indicated the reduction of plasmon

loss in the doped graphene flake. Another important characteristic was that the separations between two adjacent fringes, which approximately corresponded to half of the plasmon wavelengths $\lambda_{sp}/2$,[40] increased in the chemically-doped graphene (Fig. 3c and f). Specifically, the pristine graphene exhibited a $\lambda_{sp}/2$ of 150 nm, while the value for the doped one increases to 280 nm (Fig. 3b) and 238 nm (Fig. 3e), respectively. Because the λ_{sp} was proportional to square root of the charge carrier density ($\sqrt{n}$) in the graphene, a longer plasmon wavelength suggested increment of the charge carriers in the graphene by chemical doping.

Plasmon damping in the graphene is usually related to several mechanisms, which are radiative decay into photons, decay into electron–hole pairs *via* inter- or intraband transition, scattering with phonons of the substrate, and scattering by the disorders in the graphene.[49] According to the previous studies, the scattering of the plasmons by the disorders in the graphene are strongly dependent on the carrier density.[49,50] Presence of the disorders, such as adsorbates, impurities, defects, corrugations, and edges, will act as scattering centers for the electron oscillations and reduce the plasmon life time. With increase of the free charge carriers in the graphene, the scattering potentials from these disorder centers can be screened *via* the electron–electron interactions, whereby the plasmon damping will be reduced and therefore the plasmon life time will be increased. This mechanism is one of the origins for the low plasmon damping in the chemically-doped graphene with increased charge carriers (holes). Another reason for the low plasmon damping is due to the removal of the scattering centers from the pristine graphene during the chemical doping process. This can be verified from two aspects. Firstly, the near-field optical intensities are rather non-uniform on the pristine graphene (Fig. 3a and d). Such a non-uniformity is believed to be originated from the adsorbates, such as polymer residues and impurities, distributed randomly onto the graphene surface. These adsorbates can scatter the graphene plasmon and give weaker optical intensities at their sites. The near-field intensities become much more uniform after the HNO_3 doping (Fig. 3b and e). The calculated root-mean square of amplitude in the doped graphene is ~ 67% of that in the pristine graphene (Fig. S4[†]). This comparison strongly suggests that the adsorbates have been removed. Secondly, DFT calculations are conducted to demonstrate the possibility of removing the adsorbates by the HNO_3 treatment. To that end, the binding energy of a common adsorbate, the H_2O molecule, on the graphene surface is inspected. One can see that presence of the NO_3^- group will reduce the binding energy of the H_2O molecule (Table S1[†]). Reduction of the binding energy suggests that the adsorbate is prone to be desorbed from the graphene surface.

One intriguing characteristic of the graphene plasmon is that its dispersion is distinctly different from those in conventional two-dimensional electron gas (2DEG) systems due to the massless nature of Dirac fermions. In the long-wavelength limit the plasmon dispersion in the graphene can be analytically calculated using Drude-type conductivity,[51,52]

$$\omega_{sp} = \sqrt{\frac{e^2 E_F q}{2\pi\hbar^2 \varepsilon_0 \kappa(\omega)}} \qquad (2)$$

where q is the wavevector. The $\kappa(\omega)$ is the average dielectric function of the surrounding environment of the graphene, which can be defined as $\kappa(\omega) = (\varepsilon_1 + \varepsilon_{sub})/2$. In our current study ε_1 and

ε_{sub} are the dielectric functions of vacuum and SiO_2, respectively. The plasmon frequency ω_{sp} therefore scales as $E_F^{1/2} \propto n^{1/4}$ rather than $n^{1/2}$ in 2DEG.[10,53] The unique dispersion behavior enables extraordinary confinement of the excitation field perpendicular to the graphene flake.[19,20,54] On the other hand, the interactions between charge carriers in graphene can be screened by the adsorbates due to the atomic thickness, whereby the plasmon dispersion will be modified. It is therefore important to investigate the plasmon dispersion characteristics in chemically-doped graphene, which is essential for their utilizations in future nanophotonic devices. To this end, s-SNOM measurements were performed using different excitation wavelengths spanning from 9.60 μm to 10.70 μm. As shown in Fig. 4a–f, the normalized near-field optical amplitudes on the graphene were weakened as the excitation wavelengths were decreased. For an incidence wavelength of 9.60 μm, the optical amplitudes of the graphene and SiO_2 substrate were almost the same and one can hardly observe any plasmon fringes. This tendency is due to the fact that by reducing the incidence wavelengths, the excitations will approach optical phonon resonances of the SiO_2 and therefore the plasmon will be damped by transferring energy to the substrate phonons.[48,55]

As shown in Fig. 4g (solid lines), when the excitation wavelength was reduced the main plasmon fringes moved closer to the graphene edge and the fringe separations became smaller. Such behaviors qualitatively agreed with the predictions from Equation (2). The plasmon wavelengths were then quantitatively calculated by fitting the experimental profiles to a phenomenological cavity model describing the plasmon interference behavior.[56] Specifically, the observed plasmon fringes were resulted from the sum of the tip-launched plasmon wave and the reflected plasmon fields from the graphene edges,

$$\psi = \tilde{\psi}_{sp,0} + \sum_j \tilde{\psi}_{sp,j} \qquad (3)$$

where $\tilde{\psi}_{sp,0}$ is the tip-launched plasmon wave and

$\tilde{\psi}_{sp,j} = R_j \times \tilde{\psi}_{sp,0} \exp\left\{-\left(\frac{4\pi}{\lambda_{sp}}\right) r_j\left(\gamma_{sp} + i\right)\right\}$ describes the edge-reflected

plasmon waves. Parameters R_j, γ_{sp}, and r_j denote the reflection coefficient, plasmon damping rate, and distance between the graphene edge and AFM tip, respectively. The experimental near-field intensity was related to $|\psi|$. For all of the calculations, we fixed the $\tilde{\psi}_{sp,0}$ to 1 and took the λ_{sp} and γ_{sp} as fitting parameters. The model can describe the experimental plasmon profiles very well and give the accurate plasmon wavelengths (Fig. 4g, dashed lines), whereby the plasmon dispersion can be obtained (Fig. 4h, blue crosses).

Equation (2) was then utilized to describe the derived plasmon dispersion, where the Fermi energy E_F was treated as variable. The results indicated that excellent agreement between the theory and experiment could be obtained by choosing an E_F of 0.5 eV (Fig. 4h, blue solid line). More accurate description of the experimental results can further be done by investigating the reflection coefficient of the excitation wave by the graphene under the AFM tip, which is stated as,[57]

$$r_p(q,\omega) = 1 - \frac{\varepsilon_0}{\kappa(\omega)\varepsilon_{Gr}(q,\omega)} \qquad (4)$$

where $\varepsilon_{Gr}(q,\omega)$ is the graphene dielectric function calculated from random phase approximation (RPA) method.[53] Fig. 4h presents an intensity plot of the imaginary part of the reflection coefficient

　　　　　　　　　　　　　　　　　　　　　　　　　　　　ARTICLE

overlaid on the experimental plasmon dispersion, where excellent agreement can be obtained using an E_F of 0.5 eV. These results unambiguously demonstrate that doping of the graphene with the HNO_3 will only increase the charge carriers in the graphene while not modify the plasmon dispersion behavior.

Another important parameter that can be obtained from the cavity model is the plasmon damping rate γ_{sp}. Under the excitation at 10.70 μm, the γ_{sp} of the pristine graphene was 0.24, while that of the doped graphene was 0.16. A 34% reduction in plasmon damping can be achieved by the chemical doping, which is in line with the previous preliminary result obtained from Fig. 3 (~ 38% reduction). Fig. 4i plots the plasmon damping rate as a function of the incidence wavelength (empty squares), which indicates that the plasmon damping becomes larger for a shorter excitation wavelength. The experimental evolution of the plasmon damping rate coincided with the theoretical predictions, where the γ_{sp} was obtained from the Drude-type conductivity as $\gamma_{sp} = \mathrm{Re}(\sigma)/\mathrm{Im}(\sigma)$.[19]

It should be noted that the experimental damping rates was larger than the predicted values. This discrepancy can be ascribed to the Drude-type conductivity used, which ignored the effects of disorders, defects, and impurities on the graphene plasmon damping.[49,50]

One can calculate the carrier concentration in the graphene flake with the derived E_F. According to the relation $E_F = h v_F \sqrt{\pi n}$ (v_F is the Fermi velocity in the graphene),[4] an E_F of 0.5 eV corresponded to a hole concentration of 1.83×10^{13} cm^{-2}. If we assume that each NO_3^- group contributed one hole, then the ratio between the number of NO_3^- and carbon atoms ($N_{NO_3^-/C}$) was 1/213. DFT calculation was then utilized to scrutinize the relation between the $N_{NO_3^-/C}$ and E_F in the graphene (Fig. 5a). As shown in Fig. 5b, the calculated $N_{NO_3^-/C}$ followed a square-root-dependence on the E_F, which is in line with the relation between carrier density and Fermi energy of the graphene. In addition, the charge distribution contours clearly revealed that net positive charges can be induced in the graphene plane. These observations further corroborated the hole-doping effect induced by the HNO_3. However, for an E_F = 0.5 eV the $N_{NO_3^-/C}$ estimated from the s-SNOM experiment is relatively small in comparison with that of the DFT results. The origins of this discrepancy are not clear yet. One possible explanation is that the electronic structure of the graphene can be affected by the dipole potential induced by the adsorbed NO_3^-.
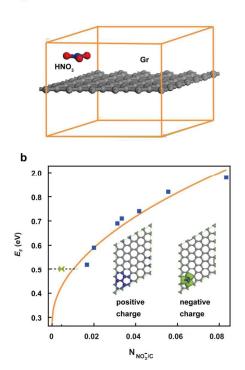
Fig. 5 First principle calculation on the HNO_3 doping of the monolayer graphene. (a) Molecule scheme used in the calculations. (b) Dependence of the E_F on the $N_{NO_3^-/C}$. The parameter $N_{NO_3^-/C}$ was the ratio between the number of NO_3^- group and carbon atoms in the graphene. The blue squares depicted the calculated results from the first principle method, while the orange line was fitting result using a square-root function. The green cross indicated the estimated $N_{NO_3^-/C}$ from the s-SNOM measurements, where the E_F was 0.5 eV.

We finally evaluated the stability of the chemically-doped graphene, which was important for its device applications. To that end, we compared the near-field optical intensity of the doped graphene flake that was stored in ambient condition for different periods. As shown in Fig. 6, the intensities and fringe separations of the near-field optical profiles were weakened rapidly in one week. Thereafter the changes in the plasmon fringes slowed down as the storage was prolonged. The extracted plasmon wavelength and E_F were reduced accordingly (Fig. 6, inset), suggesting that the holes in the graphene were annihilated gradually by the oxygen. For the damping rate, it was first increased and then stabilized after three weeks (Fig. 6, inset). The plasmon fringes became stable after ~ 7 weeks.
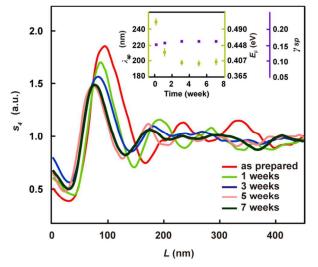
Fig. 6 Plasmon fringes extracted from the near-field optical images of the chemically-doped graphene that was stored in air for different periods. Inset shows the evolution of the plasmon wavelength λ_{sp}, E_F, and damping rate γ_{sp} over time.

3 Conclusions

In conclusion, we have systematically studied the optical properties of the chemically-doped graphene using mid-infrared nano-imaging technique, whereby the near-field plasmonic characteristics of the graphene after doped with HNO_3 can be directly visualized. The results clearly indicated that the chemical treatment can lead to p-type doping of the graphene, which thereafter enhanced the graphene plasmon oscillations and reduced the plasmon damping. In comparison with the pristine graphene, the reduction of the plasmon damping rate in the doped graphene can reach 34%. In addition, the dopants will not screen the charge carrier dynamics in the graphene. As a result the plasmon dispersion of the chemically-doped graphene still followed the evolution predicted by a Drude-type conductivity. We further evaluated the stability of the chemically-doped graphene, which showed that the improved plasmon characteristics decayed rapidly in one week and became stable after $\sim$ 7 weeks. We believe that our study can on one hand provide important insight into the understanding of improving plasmonic characteristics in graphene *via* chemical doping, and on the other hand pave the way for efficient mid-infrared optoelectronic devices using the graphene.

4 Experiment sections

4.1 Sample preparation

Single-crystalline monolayer graphene was grown on 180-μm thick Pt foils (99.9 wt % metal basis, 10 mm × 20 mm) using ambient-pressure CVD method.[37] The flow rate of the reaction gas and reaction temperature were finely controlled to obtain single-crystalline graphene flake with domain size of $\sim$ 400 μm.

The graphene was transferred onto a Si substrate with 290-nm oxide layer using the electrochemical bubbling transfer method,[38] followed by thermal annealing in Ar/H_2 ambience (400/200 sccm) at 450 ºC for 2 h to remove the organic residues. The chemical doping was conducted by exposing the graphene-covered Si substrate to HNO_3 vapor (68% in volume). The sample was placed with the

graphene facing the acid vapor. The separation between the HNO_3 solution and sample surface was $\sim$ 5 cm. The exposure lasted for more than 12 hours to ensure a uniform doping of the graphene.

4.2 Characterizations

Raman spectroscopy measurements were carried out in situ during the hydrogenation using a confocal Raman microscope (Renishaw inVia Reflex) with a 532-nm laser as excitation. The power of the excitation was kept below 1 mW to avoid heating effect. The XPS characterizations were performed on an ESCALAB 250Xi (Thermo-VG) X-ray photoelectron spectrometer.

The s-SNOM characterizations were conducted using a scattering-type near-field optical microscope (NeaSNOM, Neaspec GmbH). In a specific measurement, an AFM tip coated with metal layer (Arrow-IrPt, Nanoworld) was illuminated using a mid-infrared laser (Access Laser) with tunable wavelengths from 9.20 μm to 10.70 μm. The tip was vibrated vertically with frequency around 280 kHz. The backscattered light from the tip was detected via a pseudoheterodyne interferometric manner, where the scattered light was demodulated at fourth harmonic of the tip vibration frequency. The optical and morphology images of the sample can be simultaneously obtained by scanning the sample below the tip.

4.3 First principle calculations

The first principle calculations based on DFT were performed with DMol 3 code.[58,59] The exchange–correlation function was treated using the Perdew–Burke–Ernerhof Generalized Gradient Approximation.[60] Semi-core pseudopotentials were applied.[61] The density convergence tolerance in the self-consistent field calculation was set to 10^{-6}. The molecule structures were optimized until the total energy converged below $1.0×10^{-5}$ Ha and the force on atoms converged below 0.002 Ha/Bohr. An equivalent Monkhorst–Pack k grid of 15×15×1 for an 1×1 graphene unit cell was used in the structural relaxation.[62] In the static calculations, an equivalent Monkhorst–Pack k grid of 50×50×1 for a 1×1 graphene unit cell was used.

Acknowledgements

Notes and references

1   K. S. Novoselov, V. I. Fal'ko, L. Colombo, P. R. Gellert, M. G. Schwab, K. Kim, *Science*, 2012, **490**, 192–200.
2   F. Bonaccorso, Z. Sun, T. Hasan, A. C. Ferrari, *Nat. Photonics*., 2010, **4**, 611-622.
3   Q. L. Bao, K. P. Loh, *ACS Nano*, 2012, **6**, 3677-3694.
4   A. H. Castro-Neto, F. Guinea, N. M. R. Peres, K. S. Novoselov, A. K. Geim, *Rev. Mod. Phys.*, 2009, **81**, 109–162.
5   S. A. Mikhailov, K. Ziegler, *Phys. Rev. Lett.*, 2007, **99**, 016803.

6 M. Bordag, I. G. Pirozhenko, *Phys. Rev. Lett.*, 2014, **89**, 035421.

7 T. Stauber, *J. Phys.: Condens. Matter*, 2014, **26**, 123201.

8 M. Jablan, H. Buljan, M. Soljačić, *Phys. Rev. Lett.*, 2009, **80**, 245435.

9 T. Low, P. Avouris, *ACS Nano*, 2014, **8**, 1086–1101.

10 A. N. Grigorenko, M. Polini, K. S. Novoselov, *Nat. Photonics.*, 2012, **6**, 749–758.

11 F. H. L. Koppens, D. E. Chang, F. J. García de Abajo, *Nano Lett.*, 2011, **11**, 3370–3377.

12 V. W. Brar, M. S. Jang, M. Sherrott, J. J. Lopez, H. A. Atwater, *Nano Lett.*, 2013, **13**, 2541–2547.

13 T. Mueller, F. N. Xia, P. Avouris, *Nat. Photonics.*, 2010, **4**, 297–301.

14 F. N. Xia, T. Mueller, Y. M. Lin, A. Valdes-Garcia, P. Avouris, *Nat. Nanotechnol.*, 2009, **4**, 839–843.

15 P. N. Li, T. Taubner, *ACS Nano*, 2012, **6**, 10107–10114.

16 Y. L. Li, H. G. Yan, D. B. Farmer, X. Meng, W. J. Zhu, R. M. Osgood, T. F. Heinz, *Nano Lett.*, 2014, **14**, 1573–1577.

17 X. P. Li, Q. M. Zhang, X. Chen, M. Gu, *Sci. Rep.*, 2013, **3**, 2819.

18 W. Gao, J. Shu, C. Qiu, Q. Xu, *ACS Nano*, 2012, **6**, 7806–7813.

19 Z. Fei, A. S. Rodin, G. O. Andreev, W. Bao, A. S. McLeod, M. Wagner, L. M. Zhang, Z. Zhao, M. Thiemens, G. Dominguez, M. M. Fogler, A. H. Castro-Neto, C. N. Lau, F. Keilmann, D. N. Basov, *Nature*, 2012, **487**, 82–85.

20 J. N. Chen, M. Badioli, P. Alonso-González, S. Thongrattanasiri, F. Huth, J. Osmond, M. Spasenović, A. Centeno, A. Pesquera, P. Godignon, A. Z. Elorza, N. Camara, F. J. García de Abajo, R. Hillenbrand, F. H. L. Koppens, *Nature*, 2012, **487**, 77–81.

21 Z. Fei, A. S. Rodin, W. Gannett, S. Dai, W. Regan, M. Wagner, M. K. Liu, A. S. McLeod, G. Dominguez, M. Thiemens, A. H. Castro-Neto, F. Keilmann, A. Zettl, R. Hillenbrand, M. M. Fogler, D. N. Basov, *Nat. Nanotechnol.*, 2013, **8**, 821–825.

22 P. Alonso-González, A.Y. Nikitin, F. Golmar, A. Centeno, A. Pesquera, S. Vélez, J. Chen, G. Navickaite, F. H. L. Koppens, A. Zurutuza, F. Casanova, L. E. Hueso, R. Hillenbrand, *Science*, 2014, **344**, 1369–1373.

23 L. Ju, B. S. Geng, J. Horng, C. Girit, M. Martin, Z. Hao, H. A. Bechtel, X. G. Liang, A. Zettl, Y. R. Shen, F. Wang, *Nat. Nanotechnol.*, 2011, **6**, 630–634.

24 Z. Y. Fang, Y. M. Wang, Z. Liu, A. Schlather, P. M. Ajayan, F. H. L. Koppens, P. Nordlander, N. J. Halas, *ACS Nano*, 2012, **6**, 10222–10228.

25 Q. M. Zhang, X. P. Li, M. M. Hossain, Y. Z. Xue, J. Zhang, J. C. Song, J. Y. Liu, M. D. Turner, S. H. Fan, Q. L. Bao, M. Gu, *Sci. Rep.*, 2014, **4**, 6559.

26 A. Woessner, M. B. Lundeberg, Y. D. Gao, A. Principi, P. Alonso-González, M. Carrega, K. Watanabe, T. Taniguchi, G. Vignale, M. Polini, *Nat. Mater.*, 2015, **14**, 421–425.

27 A. M. Dubrovkin, J. Tao, X. C. Yu, N. I. Zheludev, Q. J. Wang, *Sci. Rep.*, 2015, **5**, 09837.

28 A. Kasry, M. A. Kuroda, G. J. Martyna, G. S. Tulevski, A. A. Bol, *ACS Nano*, 2010, **4**, 3839–3844.

29 S. Y. Shin, N. D. Kim, J. G. Kim, K. S. Kim, D. Y. Noh, K. S. Kim, J. W. Chung, *Appl. Phys. Lett.* 2011, **99**, 082110.

30 Y. X. Zhou, X. L. Xu, F. R. Hu, X. L. Zheng, W. L. Li, P. H. Zhao, J. T. Bai, Z. Y. Ren, *Appl. Phys. Lett.*, 2014, **104**, 051106.

31 M. Qi, Y. X. Zhou, F. R. Hu, X. L. Xu, W. L. Li, A. R. Li, J. T. Bai, Z. Y. Ren, *J. Phys. Chem. C*, 2014, **118**, 15054–15060.

32 H. T. Liu, Y. Q. Liu, D. B. Zhu, *J. Mater. Chem.*, 2011, **21**, 3335–3345.

33 H. G. Yan, Z. Q. Li, X. S. Li, W. J. Zhu, P. Avouris, F. N. Xia, *Nano Lett.*, 2012, **12**, 3766–3771

34 H. G. Yan, X. S. Li, B. Chandra, G. Tulevski, Y. Q. Wu, M. Freitag, *Nat. Nanotechnol.*, 2012, **7**, 330–334.

35 P. Alonso-González, P. Albella, F. Neubrech, C. Huck, J. Chen, F. Golmar, F. Casanova, L. E. Hueso, A. Pucci, J. Aizpurua, R. Hillenbrand, *Phys. Rev. Lett.*, 2013, **110**, 203902.

36 J. Zuloaga, P. Nordlander, *Nano Lett.*, 2011, **11**, 1280–1283.

37 T. Ma, W. C. Ren, Z. B. Liu, L. Huang, L. P. Ma, X. L. Ma, *ACS Nano*, 2014, **8**, 12806–12813.

38 L. B. Gao, W. C. Ren, H. L. Xu, L. Jin, Z. X. Wang, T. Ma, *Nat. Commun.* 2012, **3**, 23–25.

39 R. Hillenbrand, F. Keilmann, *Phys. Rev. Lett.*, 2000, **85**, 3029–3032.

40 J. N. Chen, M. L. Nesterov, A. Y. Nikitin, S. Thongrattanasiri, P. Alonso-González, T. M. Slipchenko, F. Speck, M. Ostler, T. Seyller, I. Crassee, F. H. L. Koppens, L. Martin-Moreno, F. J. García de Abajo, A. B. Kuzmenko, R. Hillenbrand, *Nano Lett.*, 2013, **13**, 6210–6215.

41 H. Z. Geng, K. K. Kim, K. P. So, Y. S. Lee, Y. Chang, Y. H. Lee, *J. Am. Chem. Soc.*, 2007, **129**, 7758–7759.

42 S. Das, P. Sudhagar, E. Ito, D. Y. Lee, S. Nagarajan, S. Y. Lee, Y. S. Kang, W. Choi, *J. Mater. Chem.*, 2012, **22**, 20490–20497.

43 S. Bae, H. Kim, Y. Lee, X. F. Xu, J. S. Park, Y. Zheng, J. Balakrishnan, T. Lei, H. R. Kim, Y. I. Song, Y.-J. Kim, K. S. Kim, B. Özyilmaz, J.-H. Ahn, B. H. Hong, S. Iijima, *Nat. Nanotechnol.*, 2010, **5**, 574–578.

44 D. M. Basko, S. Piscanec, A. C. Ferrari, *Phys. Rev. B*, 2009, **80**, 165413.

45 A. Das, S. Pisana, B. Chakraborty, S. Piscanec, S. K. Saha, U. V. Waghmare, K. S. Novoselov, H. R. Krishnamurthy, A. K. Geim, A. C. Ferrari, A. K. Sood, *Nat. Nanotechnol.*, 2008, **3**, 210–215.

46 Y. M. Shi, X. C. Dong, P. Chen, J. L. Wang, L. J. Li, *Phys. Rev. B*, 2009, **79**, 115402.

47 A. Huber, N. Ocelic, T. Taubner, R. Hillenbrand, *Nano Lett.*, 2006, **6**, 774–778.

48 A. Y. Nikitin, P. Alonso-González, S. Vélez, S. Mastel, A. Centeno, A. Pesquera, A. Zurutuza, F. Casanova, L. E. Hueso, F. H. L. Koppens, R. Hillenbrand, *Nat. Photonics*, 2016, **10**, 239–243.

49 H. Yan, T. Low, W. Zhu, Y. Wu, M. Freitag, X. Li, F. Guinea, P. Avouris, F. Xia, *Nat. Photonics*, 2013, **7**, 394–399.

50 A. Principi, G. Vignale, M. Carrega, M. Polini, *Phys. Rev. B*, 2013, **88**, 121405(R).

51 E. H. Hwang, S. Das Sarma, *Phys. Rev. B.* 2007, **75**, 205418.

52 B. Wunsch, T. Stauber, F. Sols, F. Guinea, *New J. Phys.*, 2006, **8**, 318.

53   S. Gangadharaiah, A. M. Farid, E. G. Mishchenko, *Phys. Rev. Lett.*, 2008, **100**, 166802.

54   L. Novotny, B. Hecht, O. Keller, Cambridge University Press: New York. 2006.

55   X. X. Yang, F. Zhai, H. Hu, D. B. Hu, R. N. Liu, S. P. Zhang, M. T. Sun, Z. P. Sun, J. N. Chen, Q. Dai, *Adv. Mater.*, 2016, **28**, 2931–2938.

56   J. A. Gerber, S. Berweger, B. T. O'Callahan, M. B. Raschke, *Phys. Rev. Lett.* 2014, **113**, 055502.

57   Z. Fei, G. O. Andreev, W. Z. Bao, L. F. M. Zhang, A. S. McLeod, C. Wang, M. K. Stewart, Z. Zhao, G. Dominguez, M. Thiemens, M. M. Fogler, M. J. Tauber, A. H. Castro-Neto, C. N. Lau, F. Keilmann, D. N. Basov, *Nano Lett.*, 2011, **11**, 4701–4705.

58   B. Delley, *J. Chem. Phys.*, 1990, **92**, 508–517.

59   B. Delley, *J. Chem. Phys.* 2000, **113**, 7756–7764.

60   J. P. Perdew, K. Burke, M. Ernzerhof, *Phys. Rev. Lett.*, 1996, **77**, 3865.

61   B. Delley, *Phys. Rev. B*, 2002, **66**, 155125.

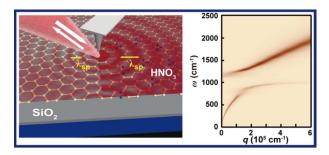62   H. J. Monkhorst, J. D. Pack, *Phys. Rev. B*, 1976, **13**, 5188.

Graphical Abstract

Chemically-Doped Graphene with Improved Surface Plasmon Characteristics: An Optical Near-field Study

Zebo Zheng,[ad] Weiliang Wang,[d] Teng Ma,[c] Zexiang Deng,[d] Yanlin Ke,[ab] Runze Zhan,[a] Qionghui Zou,[ad] Wencai Ren,[c] Jun Chen,[ab] Juncong She,[ab] Yu Zhang,[ab] Fei Liu,[ab] Huanjun Chen,[ab*] Shaozhi Deng,[ab*] Ningsheng Xu[ab]

- [a.] [†] State Key Laboratory of Optoelectronic Materials and Technologies, Guangdong Province Key Laboratory of Display Material and Technology, Sun Yat-sen University, Guangzhou 510275, China.
- [b.] School of Electronics and Information Technology, Sun Yat-sen University, Guangzhou 510006, China.
- [c.] Shenyang National Laboratory for Materials Science, Institute of Metal Research, Chinese Academy of Sciences, 72 Wenhua Road, Shenyang 110016, China.
- [d.] School of Physics, Sun Yat-sen University, Guangzhou 510275, China
- [*] Corresponding Authors: chenhj8@mail.sysu.edu.cn; stsdsz@mail.sysu.edu.cn

The surface plasmon characteristics of chemically-doped graphene were systematically studied using the scanning near-field optical technique.